Heliyon 9 (2023) e18519

Contents lists available at ScienceDirect

Heliyon

journal homepage: www.cell.com/heliyon

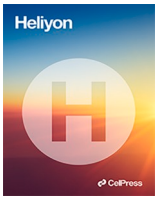

Structure and magnetic properties of $SiO_2 - FeO - CaO - Na_2O$ bioactive glass-ceramic system for magnetic fluid hyperthermia application

P. Rastgoo Oskoui, M. Rezvani *

Department of Materials Engineering, University of Tabriz, Tabriz, Iran

ARTICLE INFO

Keywords:
Hyperthermia
Glass-ceramic
Magnetic
Sol gel
Simulated body fluid

ABSTRACT

Ferrimagnetic glass-ceramics comprising maghemite crystals were synthesized for magnetic fluid hyperthermia (MFH) usage. The present work is focused on the result of the chemical composition and heat treatment temperature on the magnetic behavior of $(60-x)SiO_2 - (10+x)FeO - 20CaO - 10Na_2O, 0 \leq x \leq 30$ glass-ceramic system. It was observed that with the increasing of FeO from 10 to 40 wt% in the glass-ceramic compound, the percentage of maghemite phase increased. It was also seen that in the low heat treatment temperature (680 $^{\circ}C$), by adding iron oxide up to 30 wt%, iron cations acts as a network former, and more than this amount acts as a network modifier. In contrast, iron cations in the same composition range at high temperatures (840 $^{\circ}C$), acts as a network modifier. According to the VSM results, the maximum magnetization of glass-ceramics incremented from 0.23 emu/g to 0.30 emu/g with the increase in FeO percentage. It was also observed that with the increment of iron oxide percentage, the morphology of maghemite crystals changed from spherical to dumbbell-shaped.

1. Introduction

Among conventional methods treatment of cancer, hyperthermia is a hopeful and successful approach to cancer treatment [1]. Currently clinical hyperthermia treatment using regional perfusion with warm blood, microwave, ultrasound, or any other source of electromagnetic energy is used [2–5]. But the most important problem in using these ways are the spinosity of controlling local tumor heating without damage a normal tissue [6]. In addition, in most of these treatment methods, invasive heat is used [7]. It is been reported that magnetic bioactive glass-ceramics can heat the cancer cell without damaging the normal tissue [8].

The method includes focusing on magnetic bioactive glass-ceramics to tumor tissue accompanied with the utility of an outside alternating magnetic field that induces heat via hysteresis losses of the magnetic bioactive glass-ceramics [9]. Incrementing the temperature of the cancerous tissue up to 43 $^{\circ}C$ causes the necrosis of most cancer cells, but this increase in temperature does not damage the surrounding normal tissue [10].

It is known that the heat production in this method pertain on the magnetic properties of the magnetic bioactive glass-ceramics particles, magnetic field parameters and the specification of the cancerous tissue [11]. Important part of the thermoseeds for magnetic fluid hyperthermia is to achieve the favorable magnetic properties of the thermoseeds [12].

Bretcanu et al., in 2006 investigated the magnetic properties of $SiO_2 - FeO - Fe_2O_3 - Na_2O - CaO$ glass-ceramic system melted at

* Corresponding author.
E-mail address: m_rezvani@tabrizu.ac.ir (M. Rezvani).

https://doi.org/10.1016/j.heliyon.2023.e18519
Received 8 May 2023; Received in revised form 18 July 2023; Accepted 19 July 2023
Available online 2 August 2023

different temperatures. Magnetite and hematite were the main crystallized phases in glass-ceramics. Largest hysteresis loop area was obtained for the melted sample at 1500 °C. Magnetic hysteresis loop area directly correlates with the amount of losses. In their study, the highest loss is related to the sample melted at 1500 °C. With the increase in losses, the amount of heat produced by the glass-ceramic placed in the alternating magnetic field also increases. The maximum amount of magnetic losses (61 W/g) for the samples melted at a temperature of 1500 °C has been obtained, which can increase the temperature by 87 °C [13].

Shah et al., in 2009 prepared xZnO·(40−x) SiO_2·25CaO·25 Fe_2O_3 7P2O5·3 Na_2O glass-ceramic by the melt-quench process. Their studies showed that hysteresis area and saturation magnetization enhancement with the increment in ZnO content [14].

Wang et al., in 2013 studied the magnetic behavior of $10Li_2O - 35SiO_2 - 16Fe_2O_3 - 9MnO_2 - 25CaO - 5P_2O_5$ (10LFS) glass. Heat treatment of glasses was done at 850°C , and wollastonite and magnetite were seen as the main crystallized phases in the glass field. In the investigation, it was observed that heat treatment at 850 °C for 16 h under an applied field (1000 Oe) resulted in a very small residual magnetism of 0.01 emu. g^{-1} because of the presence of magnetite [15].

Leenakul et al. in 2015, investigated the effect of adding $BaFe_{12}O_{19}$ to the $SiO_2 - Na_2O - P_2O_5 - CaO$ glass system by a modified solid-state sintering method. In phase studies, $Na_6Ca_3Si_6O_{18}$ and $BaFe_{12}O_{19}$ (BF) phases were seen in heat-treated glasses. And it was also seen that glass-ceramics bioactivity recovered with incrementing barrium ferrite content [16].

Shabrawy et al., in 2016 studied the crystallization behavior of $K_2O - MgO - B_2O_3 - P_2O_5 - Fe_2O_3$ glass-ceramic system. The glass-ceramics of the system was synthesized by melting method. Heat treatment of glasses was done at temperatures between 560 °C and 700 °C some time between 2 and 8 h. $MgFe_2O_4$ phases and a small amount of hematite (α-Fe_2O_3), were seen as the main phases in glass-ceramics. With increasing temperature and heat treatment time, the amount of hematite phase also increased [17].

Wang et al., in 2016 studied the relationships among changing the chemical composition and magnetic losses of $Fe_2O_3 - SiO_2 -$ CaO glass-ceramics. The results of their research confirmed that the magnetic losses of $Fe_2O_3 - SiO_2$-CaO glass-ceramics elevated steadily with incrementing magnetite crystallization [18].

Baino et al., in 2018 prepared a CaO-Fe_2O_3-SiO_2 glass-ceramics system by sol-gel process and they studied the effect of different treatment atmosphere (air and argon flow) on the crystallization of magnetic phases. Investigations showed magnetic properties adjusted with control the iron oxide content and heat treatment atmosphere (air vs. argon atmosphere) during heat treatment [19].

According to the study conducted by Fiume et al., in 2020, bioactive sol-gel glasses show a high specific surface due to structural porosity as a result of condensation of silanol groups. As a result, sol-gel glasses show better biocompatibility compared to their melt-derived counterparts [20].

In this work, for the first time, glass-ceramic system $(60-x)SiO_2 - (10+x)FeO - 20CaO - 10Na_2O, 0 \leq x \leq 30$ with different compositions synthesized by self-catalysing sol method. The structural and magnetic phase characteristics were investigated, and eventually, in vitro bioactivity of sample was also studied.

2. Materials and method

2.1. Materials

Tetraethyl ortho silicate (TEOS, $Si(OC_2H_5)_4$; 99%, Merck), iron nitrate ($FeNO_3$; 99%, Merck), sodium nitrate ($NaNO_3$; 99.98%, Merck), and calcium nitrate tetrahydrate ($Ca(NO_3)_2.4H_2O$; 99.5%, Merck) used as silicon, iron, sodium, and calcium sources, respectively. Ethanol (C_2H_5OH; 99%, Merck) and distilled water were used as solvents.

2.2. Synthesis of sol-gel bioactive glass

Glass-ceramics have been synthesized by self-catalyzed sol method [21]. The method of preparation of the sol is explained briefly. In the first step, a solution of tetraethyl orthosilicate was prepared in ethanol. Then a solution of $Ca(NO_3)_2.4H_2O$ was added to the sol at room temperature and stirred for 20 min. Then sodium nitrate solution in water added to the sol and continued stirring for 20 min. In the next step, iron nitrate solution in ethanol was spilled to the sol, and stirring was continued for 1 h to obtain a homogeneous sol (in the preparation of sol, the precursor to solvent ratio was chosen as 1:5, and the temperature of the sol was kept constant at 25 °C). The sols were aged at room temperature in a closed container for 24 h. The synthesized sols were dried at 110 °C and heat treated at 680 °C and 840 °C for 2 h. The chemical composition of the synthesized glass-ceramics is given in Table 1.

Table 1
Chemical composition of synthesized glass.

Sample code	Chemical composition of samples (wt%)
G40 F	$30SiO_2 - 40FeO - 20CaO - 10Na_2O$
G30F	$40SiO_2 - 30FeO - 20CaO - 10Na_2O$
G20F	$50SiO_2 - 20FeO - 20CaO - 10Na_2O$
G10F	$60SiO_2 - 10FeO - 20CaO - 10Na_2O$

2.3. Sample analysis

The prepared G30F gel sample was analyzed by differential thermal analysis (DTA-SDTQ600-TA Instruments, USA) to determine the crystallization temperatures. For this, 22 mg of dried gel with a particle size below 30 μm was placed inside the alumina crucible, and analytical-grade alumina powder was used as a reference. The study of specimen crystalline phases was done using X-ray powder diffraction analysis (XRD, PANalytical PW3830, Netherlands). A Cu-Kα irradiance source (λ = 0.5406 Å) were scanned at 45 kV and 31 mA in the range of 2θ-range of 5–75 ° at a speeding of 3 °/min. Diffraction peaks were investigated, and crystalline phases were analyzed using XPert High Score Plus software based on JCPDS sources. FTIR spectroscopy of heat-treated glass-ceramic at different temperatures is done by a JASCO FT/IR-310E spectrophotometer (JASCO, Japan). Samples were prepared using the KBr technique at room temperature in the range of 400–4000 cm^{-1}. Magnetic properties of samples by a vibrating sampler Magnetometer (VSM, Lake Shore 7620) were measured at room temperature. In order to study the bioactivity of glass-ceramics, the samples were immersed in a simulated body fluid (prepared according to the Kokubo protocol) and after a certain period of time, specimen were removed from the solution and analyzed [22].

A Digital Benchtop Water Quality pH Meter (Piccolo; Hanna Instruments Japan, Tokyo) was used to measure the pH of the SBF solution. Examination of the microstructure of the specimens and the morphology of the crystallized phases during heat treatment at 690 °*C* was seen using a scanning electron microscope (SEM/EDS, Quanta FEG 250, Netherlands) that worked with an acceleration voltage of 20 kV.

To measure the fluid temperature increase by the synthesized glass-ceramic under the magnetic field, AC hyperthermia magnetic system was designed and built. A glass tube to hold the sample was put in the middle of the coil (the coil is designed to produce an induced magnetic field in the form of a sine wave with $H_{max} = 380$ Oe and f = 380 kHz). The cold water circulation system around the coil kept its temperature constant up to 21 °C. Temperature was measured using an optical thermometer. In order to check the amount of heat loss, 4 g of synthesized glass-ceramic powder were spilled into 10 ml of distilled water and placed in the coil. The temperature increase of the samples was measured in different time intervals.

3. Results and discussion

3.1. Thermal and structural behavior of glass-ceramics

The DTA curve of $40SiO_2 - 30FeO - 20CaO - 10Na_2O$ gel prepared at 100–1100 °C is shown in Fig. 1. According to the theory of crystallography, the deposition of crystal nuclei is an endothermic process. It absorbs the required energy from the environment, while crystallization is an exothermic process, and during crystallization, a phase changes from an unstable state to a stable state. As a result, the endothermic and exothermic peaks in the DTA curve, indicate the glass nucleation and crystallization processes, respectively [23–26].

In the DTA curve two apparent crystallization peaks can be observed: The first crystallization peak (T_{c1}) at about 500–780 °C is attributable to the crystallization of the maghemite (γ - Fe_2O_3), sodium-calcium silicate, and maghemite to hematite (α- Fe_2O_3) transformation. The thermal transformation from maghemite to hematite due to the stability of the hexagonal phase than the cubic phase in 570–690 °C [27–29]. The second crystallization peak (T_{c2}) at about 790–940 °C is assigned to the crystallization of the wollastonite phase, as confirmed with the aid of the XRD patterns.

XRD patterns of dried gel and heat-treated specimens for 2 h in air atmosphere are indicated in Fig. 2. XRD patterns of dried gel at 110 °*C* with various compositions are shown in Fig. 2. (a). No sharp crystal peaks can be seen in the XRD pattern, that shows the

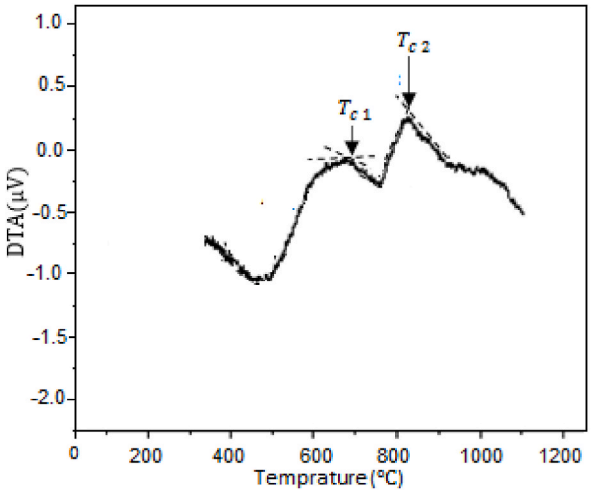

Fig. 1. The DTA pattern of $\mathbf{40SiO_2 - 30Fe_2O_3 - 20CaO - 10Na_2O}$ gel sample.

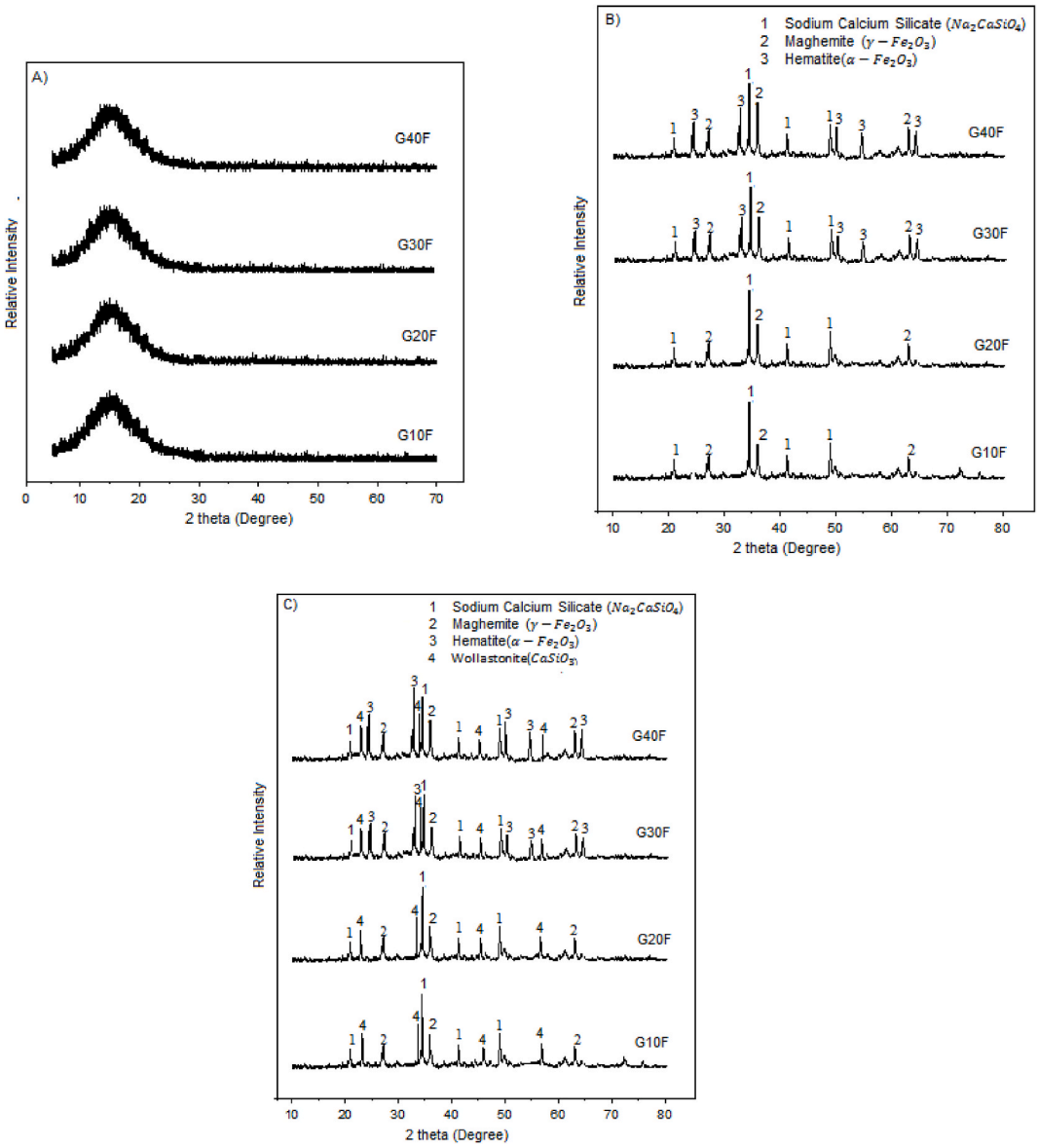

Fig. 2. XRD Patterns Synthesized glass samples and heat-treated glass-ceramic for 2 h an air atmosphere. (a) samples dried at 110 °*C*, (b) heat-treatment glass-ceramic at temperature 687 °*C*, and (c) heat treatment glass-ceramic at temperature 840 °*C*.

amorphous nature of the specimen. The XRD patterns of heat treatment glass-ceramics at 680 °*C* in air atmosphere for 2 h are shown in Fig. 2. (b). In samples, S10F and S20F, Na_2CaSiO_4 phase and γ - Fe_2O_3 peaks observed. Na_2CaSiO_4 is a bioactive silicate, and the main components in this composition (Na_2O, CaO, and SiO_2) are very like to the composition of bioactive compound [30,31]. Na_2CaSiO_4 crystallization can increase the biocompatibility of synthesized glass-ceramics [32].

On the other hand, with the increase of iron oxide percentage in S30F and S40F samples, in addition to sodium calcium silicate peaks and maghemite, hematite peaks are also seen in the glass, and it was also considered that with increasing of iron oxide percentage, the percentage of maghemite and hematite phase has increased. Maghemite has the chemical formula γ - Fe_2O_3 and a spinel crystal structure [33]. Fe^{3+} cations are randomly located in 16 octahedral and 8 tetrahedral sites within the FCC packing of oxygen anions. The magnetic response of maghemite depends on the number of Fe^{2+} cation vacancies (⊗) in the octahedral position and their arrangement. When the vacancies are randomly distributed in the maghemite crystal structure, its space group is Fd3m. The formula unit is written as $(Fe^{3+})_8^{tetr}[Fe^{3+}_{5/3}\otimes_{1/3}]_8^{oct}O_{32}$, which is the crystal arrangement of normal spinel. Since the spins in the tetrahedral and octahedral sites are orientated anti-parallel, maghemite is ferrimagnetic [34,35]. As the temperature increases, maghemite turns into hematite, which consists of twins. The transformation orientation relationship is [110]γ//[0110]α and (111)γ//(0001)α. The twinning plane of the transformation product was determined to be (0110) Plane. The mechanism of transformation of maghemite to hematite

includes the re-accumulation of close oxygen ion layers and the simultaneous displacement of iron ions that are placed in the oxygen gap [36,37]. Hematite crystallizes in the rhombohedral lattice system, and it has an identical crystal structure to corundum, which includes the sequence of Fe^{3+} caions in octahedral coordination and Oxygen anions are placed in the closest hexagonal packing positions [38]. Hematite exhibits a complex magnetic behavior. At temperatures lower than −193 °C, hematite has antiferromagnetic behavior, and when the temperature increases to −13 °C, it undergoes a Morin transition, which includes a spin flip that leads to weak ferromagnetic properties, and as the temperature increments to temperatures above 681 °C (Curie temperature), it shows paramagnetic properties. In the structure of hematite, it can be imagined that the Fe–O3–Fe units (triplets) of oxygen atoms are located close to Fe(III) on both sides, and the Fe(III) atoms in each of these triple units have the spins are opposite, and Consequently the superexchange interaction through three oxygen atoms, the iron (III) atoms are antiferromagnetically coupled and make hematite antiferromagnetic, and due to the low symmetry in the cationic positions, spin-orbit coupling is possible, which results in a deviation in moments where the plane is perpendicular to the c-axis. With decreasing temperature at −13 °C due to the change in anisotropy, the disappearance of the moment happens, which causes the moments to align along the c-axis [39–42].

Fig. 1(c) shows the XRD patterns of treated specimen at 810 °C for 2 h in air atmosphere. The results indicated that with the increment the treatment temperature, the relative intensity of maghemite and hematite phase has decreased and increased, respectively. Furthermore, with increasing the temperature of heat treatment, in addition to hematite, maghemite, and sodium calcium silicate crystals, wollastonite crystals have also crystallized in the samples. Wollastonite ($CaSiO_3$), is a biodegradable phase and is effortlessly biodegradable. Its insoluble substances (Ca and Si) assist bone cells growth and function, and these phase will increase the biocompatibility of the samples.

The size of hematite, maghemite, and sodium calcium silicate crystals in heat-treated glass-ceramics at different temperatures was calculated using Scherer's equation. The calculated crystallite sizes are shown in Table 2.

$$D = \frac{K\lambda}{\beta\, Cos\, \theta} \tag{1}$$

Where D is the size of the crystals (nm), K is Scherer's constant and it's value equal to 0.94. λ is the wavelength of the X-ray source and its value is 0.154 nm, β is the full width at half maximum in radians, and θ is the peak position in radians [43].

Fig. 3 (a) presents the FTIR spectrum of the specimens treated at 680 °C for 2 h in which the peaks centered at 1016 cm^{-1}, 928 cm^{-1}, 708 cm^{-1} and 454 cm^{-1} have strong absorption ability. The maximum and broadest band has been located at about 1016 cm^{-1}, belongs to Si–O–Si bending vibrations [44,45]. The width of the band is a function of the homogeneity of the chemical bond, and the presence of any defect causes strain in the chemical bonds, which changes the strength of the bond and shows its effect in small displacements of the bond positions. The observed band relevanted to the asymmetric stretching of Si–O–Si shifts to lower wavenumbers by incrementing the percentage of iron oxide in the sample.

The band located in wave number near 928 cm^{-1}, related with the stretching of $Si-O-Na^{+}$. And by incrementing the amount of iron oxide in the glass network from 10 to 30% by weight, this band changes to lower wave numbers. These changes indicate that the iron cations in this range have acted as glass network former and reduced the number of non-bridging oxygens. While increasing the percentage of iron oxide to higher values, this band changes to higher wave numbers. This transition to higher wave numbers shows that with the increment in the percentage of iron oxide, the number of non-bridge oxygens in the glass network has increased, and it is clear that iron oxide acts as a network modifier in this range. The observed band at about 470 cm^{-1} is related the tetrahedral bending vibrations of SiO_4 and shifts to lower wave numbers with the decrease of silica percentage in the glass network.

Fig. 3 (b) Indicated the FTIR spectra of heat-treated specimens for 2 h at 840 °C. The band seen at the wave number near 1016 cm^{-1} is associated to the asymmetric stretching of Si–O – Si and similar to the FTIR patterns of heat-treated samples at 680 °C; this bond also shifts to lower wave numbers with increasing iron oxide present in samples. This transition in the position of the band indicatesthe textural changes in the sample with increasing iron oxide percent. The band located around the wave number of 928 cm^{-1} is related to the stretching of $Si-O-Na^{+}$. A great difference is seen compared to the FTIR spectra of the specimens treated at 680 °C. It can be find out that with the increase of the percentage of iron oxide from 10 to 40% by weight, this band changes to higher wave numbers, which means that iron ions act as a glass network modifier at high temperature.

Table 2
Calculated crystallite size for $(60-x)SiO_2-(10+x)FeO-20CaO-10Na_2O, 0 \le x \le 30$ glass-ceramic system treated at various temperatures.

Sample Code	γ - Fe_2O_3	α - Fe_2O_3	Na_2CaSiO_4	Heat-treatment Temperature (°C)
G10F	18	–	25	687
G20F	26	–	26	687
G30F	42	26	28	687
G40F	54	31	24	687
G10F	21	–	36	840
G20F	29	–	35	840
G30F	19	74	34	840
G40F	30	88	38	840

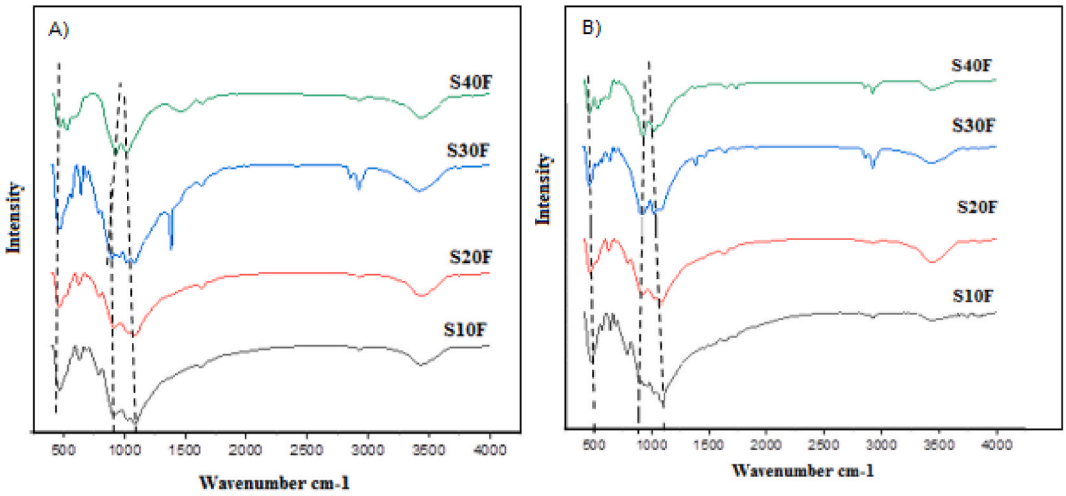

Fig. 3. FTIR spectra of glass-ceramic heat-treated at (a) 680 °C (b) **40**°*C* .

3.2. Magnetic properties of glass-ceramics

VSM curves are indicated in Fig. 4. All four glass-ceramic specimens showed alike magnetic type. All curves have a low coercive field (≅ 150 Oe) and thin hysteresis cycle, characteristic of soft magnetic materials. The saturation magnetization ranges from 0.23 emu/g for G10F to 0.3 emu/g for G40F, and the coercive field ranges from 142 Oe for G20F to 96 Oe for G40F and the residual magnetization for G40F is about fourteen times as large as for G10F. The reported results are summarized in Table 3.

Maghemite is a ferrimagnetic material with a pure magnetic moment (formula 2.5 μB/unit) and a high Curie temperature (676 °C). Maghemite saturation magnetization (76 emu/g) is lower than magnetite (92 emu/g) and more than hematite (0.1–0.4 emu/g). On the other hand, the Coercive force of maghemite is similar to magnetite (50-800G) and less than hematite (1000-5000G) [46–48].

Magnetism is directly related to amount of crystallized maghemite in the specimens [49]. G40F sample contains a larger amount of magnetite and so have higher saturation magnetic value. Remanence indicates that a ferromagnetic or ferrimagnetic material can become automatically magnetized even without an external magnetic field. Generally, residual magnetic values in glass-ceramics are much less than saturated magnetic values owing to structural features. By increasing the saturation magnetization and increasing hysteresis loop area, the amount of losses in the alternating magnetic field increases. In other words, G40F glass-ceramic can be suitable for applying of magnetic fluid hyperthermia.

SEM image of glass–ceramic specimens treated at 680 °C are indicated in Fig. 5(a)-5(d). The two specimens (G10F and G20F) show alike characteristics and it can be seen that maghemite is crystallized spherically and with the increase of the FeO percentage in the composition of specimen, the size of the crystals increases.

It can be observed that with the increasing percentage of iron oxide in glass-ceramic samples, maghemite crystallized in a dumbbell shape. In addition, with the incrementing the percentage of iron oxide, the dumbbell-shaped structure became finer. In both samples, the cubic morphology of hematite can be seen, and with the increment in the percentage of iron oxide, unlike maghemite, the hematite crystals have become larger.

Magnetic hyperthermia measurement was performed to investigate the heat production ability of synthesized glass-ceramics under

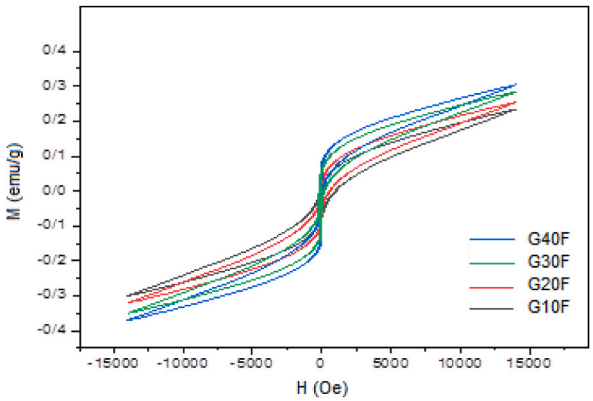

Fig. 4. VSM curves of glass-ceramic samples heat-treat at 680 °C.

Table 3
Magnetic parameters estimated from hysteresis cycles for glass-ceramic powders.

Magnetic parameters	G10F	G20F	G30F	G40F
Saturation magnetization, Ms (emu/g)	0.23	0.25	0.28	0.30
Coercive force, Hc (Oe)	106	144	120	96
Remanence magnetization, Mr (emu/g)	0.052	0.025	0.055	0.075
Hysteresis area ±15 kOe (erg/g)	3248	3256	3280	3320

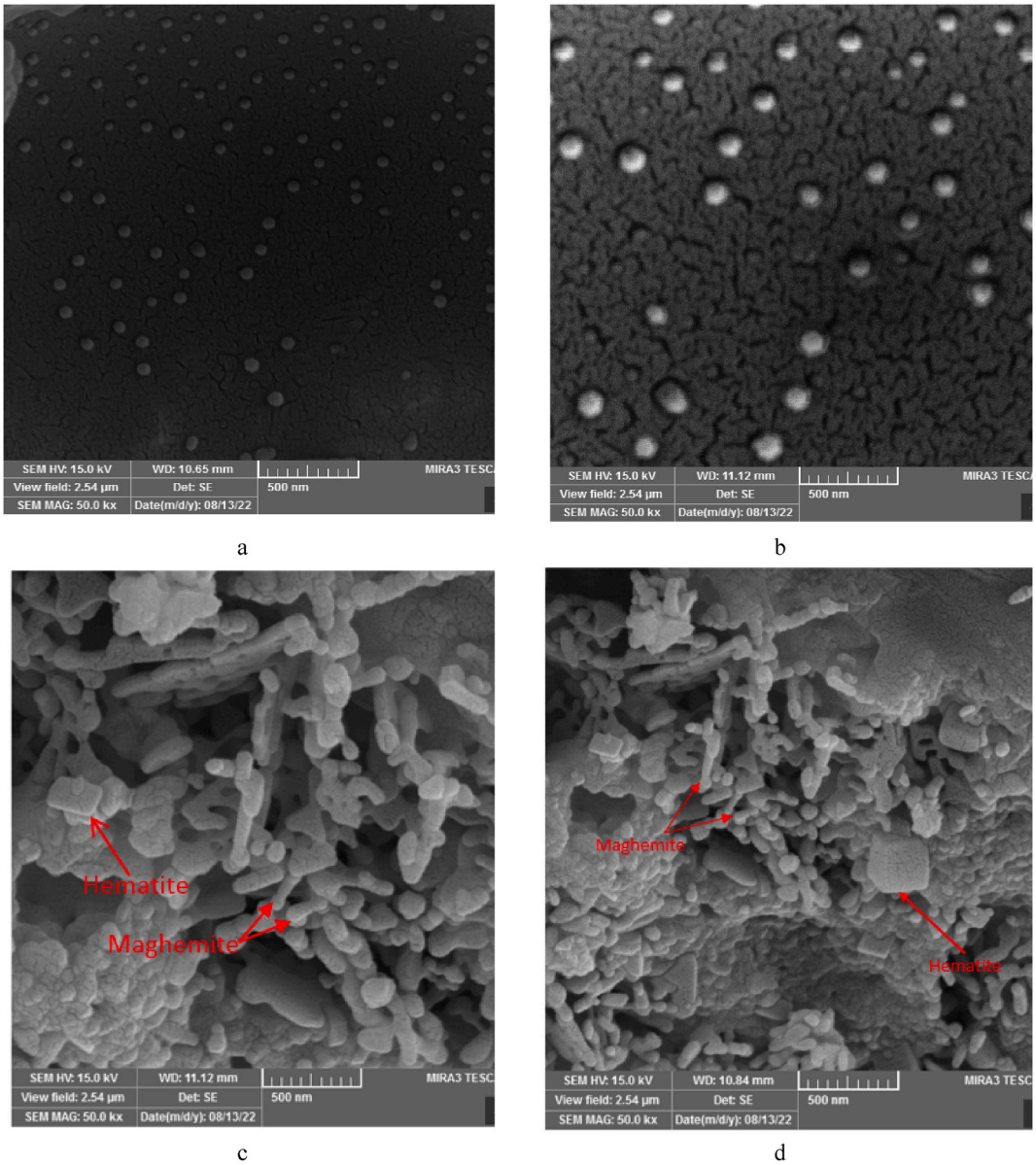

Fig. 5. SEM images of glass–ceramic samples heat-treated at 680 °C.(a) G10F, (b) G20F, (c) G30F and (d) G40F.

alternating magnetic field. Fig. 6 show the temperature changes for heat treated samples at 680 °*C*. The applied field was 335 Oe and the applied frequency was 400 kHz. The primary temperature of the all samples was 20 °*C* and it was seen that the temperature increments with time. The temperature of the water containing G40F glass-ceramic powder increased by 9 °*C*, and as a result, the maximum amount of losses was obtained. While the increase in temperature was less for the other glass ceramics. Magnetic nanoparticles, placed in an alternating magnetic, increase the temperature of the fluid by two mechanisms: Neel-Brownian relaxation and loss of hysteresis. Néel relaxation occurs as a result of fast changes in the direction of the magnetic moments comparative to the crystal

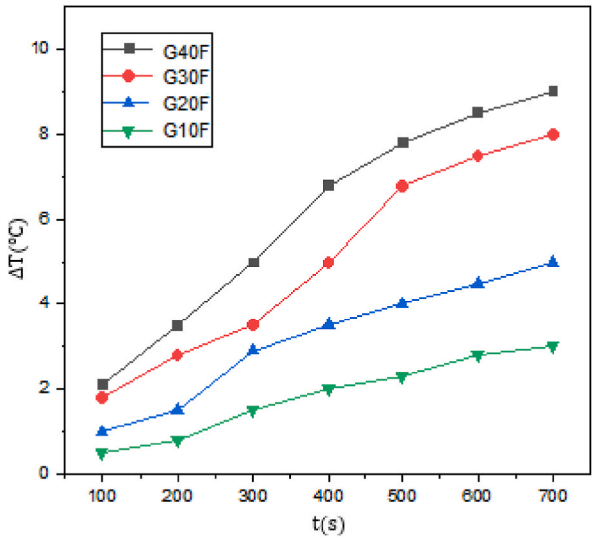

Fig. 6. Temperature changes of ferrofluid according to time in magnetic field.

lattice. But Brownian relaxation occurs as a result of the physical swirl of the glass-ceramic powder in the fluid and counteracting the motion of the particles by viscosity. Néel and Brownian relaxation occurs in the case of single-domain nanoparticles. In case of synthesized glass-ceramics, considering that the size of maghemite crystals is larger than 10 nm and is one of the multi-domain materials, the Néel and Brownian heat dissipation mechanisms can be ignored. Hysteresis losses occur in these glass-ceramics. Hysteresis losses occur due to the reciprocating movement of the magnetic domain wall in the direction of the alternating magnetic field and cause heat generation.

3.3. *In vitro bioactivity of glass-ceramics*

pH variation of G10-G40F specimens after immersing in simulated body fluid solution for up to 28 days is shown in Fig. 7. In the pH study, it was observed that in the period of 1 to 3 days, the pH value of the solution for all samples increased compared to the initial pH of the solution, which was 7.4 in physiological conditions. In SBF solution, the rapid release of Na^+, Ca^{2+} cation via exchange with H_3O^+ or H^+ ions leads to an increment in the pH value. Replacing H^+ ions with cations leads to an increment in the concentration of dissolved hydroxyl group. Cation exchange by attacking the silica network leads to the formation of silanols [50,51]. The formation of silanols in samples immersed in simulated body fluid solution for 7 to 28 days leads to a decremen in pH, as shown in Fig. 6. It can be observed that the decremen in pH increases after 14 days, which is owing to the breakdown of the glass network.

It can also be seen in Fig. 7 that by increasing the iron oxide percentage in the specimen, the pH of the SBF solution containing the

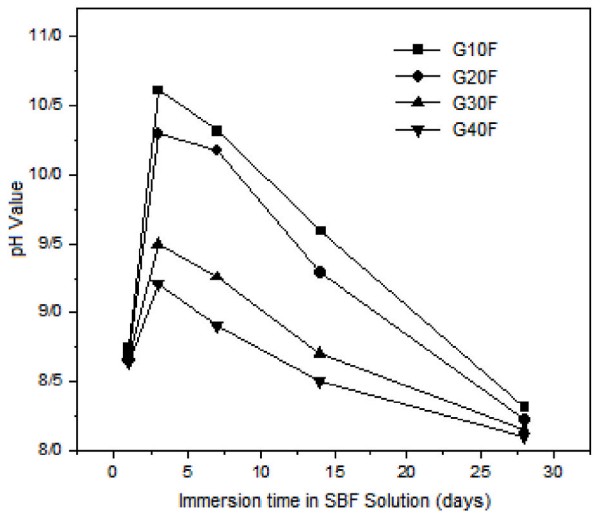

Fig. 7. pH variation of G10-G40F samples after immersing in SBF solution.

submerged specimen increment less than the other samples for three days. The pH of the simulated body fluid solution starts to decrease in all specimen after three days. In physiological conditions and owing to the rapid dissolution rate, the maximum pH values on the third day for G10-G40F samples were recorded as 10.62, 10.31, 9.49, and 9.24 at 37 °C.

Higher pH values are obtained when the rate of degradation of the glass network is higher. This increment in the pH value of simulated body fluid solution also favors the formation of hydroxyapatite carbonate. Because for bone formation, the cross-linking of collagen chains, and the deposition of hydroxyl apatite carbonate is required, and the bone formation site requires a high pH.

XRD patterns of glass-ceramic specimens treated at 680 °*C* and immersed in SBF solution for 28 days, shown in Fig. 8. After SBF treatment for 28 days, sharp peaks as to the crystallization of the hydroxyapatite phase can be observed in the diffraction patterns of all bioactive glass-ceramic samples. Also, by increment the FeO percentage in specimen and increasing the crystallization of maghemite and hematite, the intensity of the hydroxyapatite peaks has decreased. After 28 days of soaking, the intensity of the apatite peaks in sample G10F-G30F was seen to be higher and more obvious than the rest of the samples, while the peaks of sodium calcium silicate, maghemite, and hematite disappeared. That's because the formation of thick and compact apatite layers on the surface of the sample G10F-G30F happened. With the increment of FeO percentage in the glass-ceramics samples, the intensity of the apatite peaks has decreased, which is due to the presence of maghemite and hematite phases in the glass-ceramic sample. In the G40F sample, in addition to the apatite peak, small maghemite peaks are also seen, which indicates the formation of a thin layer of hydroxyapatite on the surface of the glass-ceramics.

The formation of the apatite layer on the samples immersed in the SBF solution was studied by SEM images and are shown in Fig. 9 (a)-9(d). For G10F-G40F samples, a significant HA layer observed after 28 days of soaking on the surface. It can be seen that with the increment in the FeO percentage in the samples, the crystallization rate of hydroxyapatite has decreased. Hydroxyapatite is a illustrious part of tooth enamel and bone, which has a composition of calcium hydroxyapatite and the Ca/P ratio is 1.67.

EDX analysis for the G10F sample showed that the ratio of calcium to phosphorus on the surface of the sample was about 1.69, which is close to stoichiometric apatite. EDX analysis for G20Fsample showed that the ratio of calcium to phosphorus was about 1.70, which is close to stoichiometric apatite. An increase in calcium and phosphorus levels was seen in submerged surfaces. But by an incremented in the FeO percentage in the specimen, it can be seen that the ratio of calcium to phosphorus decreased in the case of the G30F sample is 1.22. In addition, iron peaks are seen, and the intensity of the Si peak decreased. For the G40F sample, the Ca/P molar ratio equals 1.2, which corresponds to non-stoichiometric biological apatite.

Bioactivity, along with the magnetic properties of the synthesized specimens, indicate that these glass-ceramics can be used in cancer treatment by the hyperthermia treatment. Due to the good bioactivity of G40F glass-ceramic, in the treatment of bone cancer, these materials, together with the reduction of malignant tumors, may strengthen the damaged bone. Although, to make a correct decision about the suitability of existing specimens for medical usage, more advanced in vivo tests are needed.

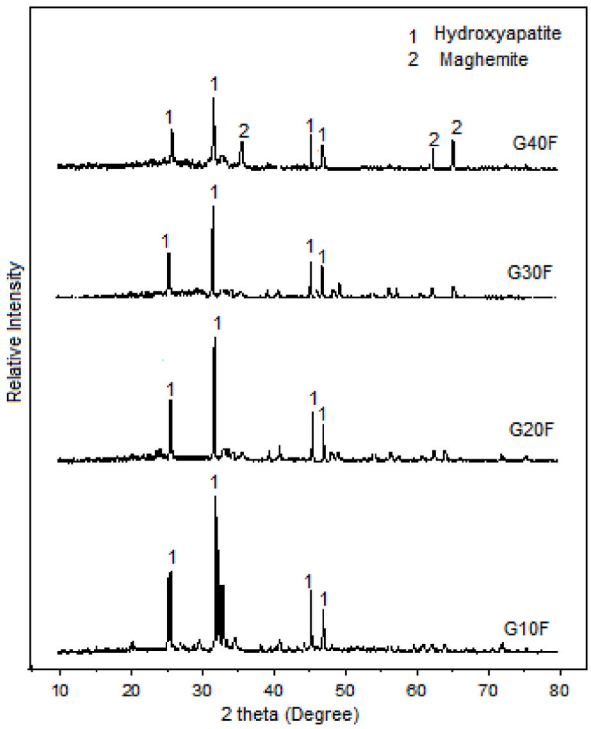

Fig. 8. XRD patterns of bioactive glass-ceramic samples heat treated at 680 °*C* and immersed in SBF solution for 28 days.

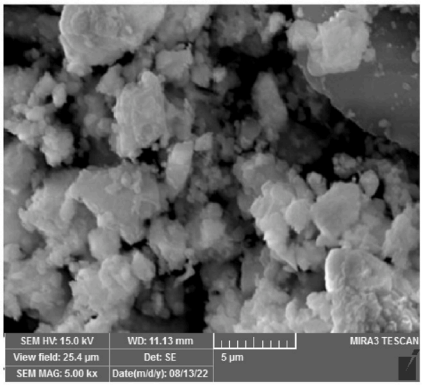

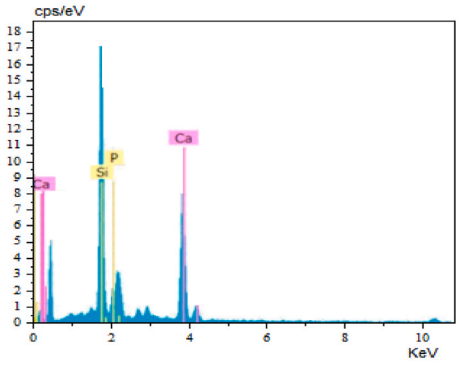

a

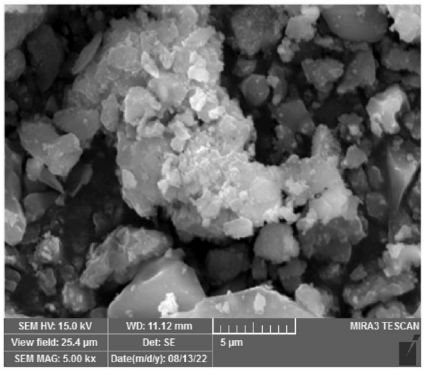

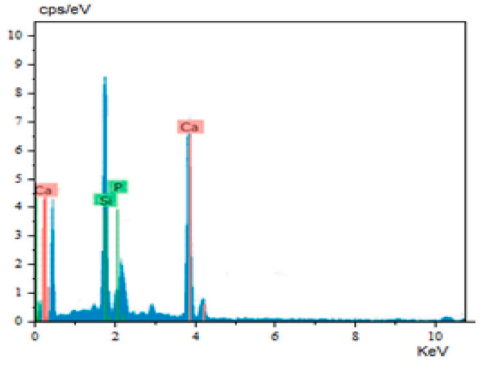

b

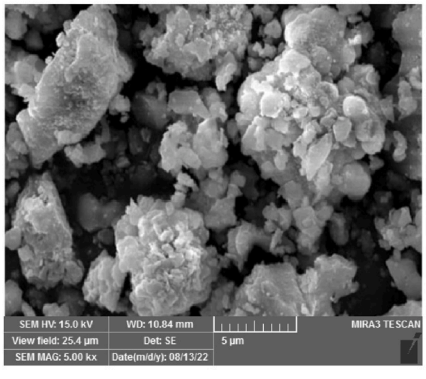

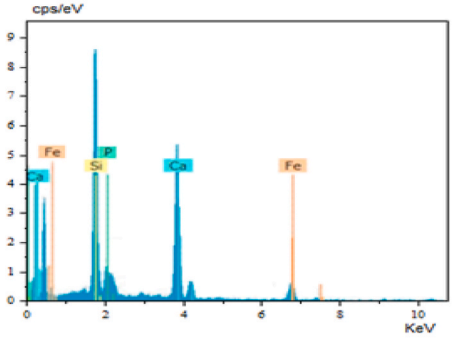

c

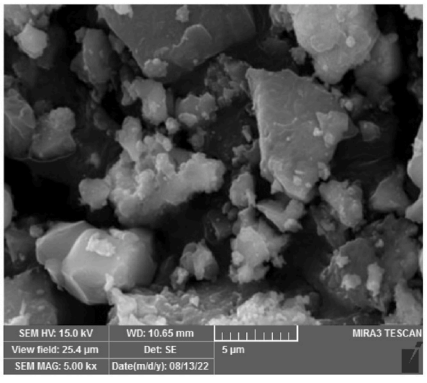

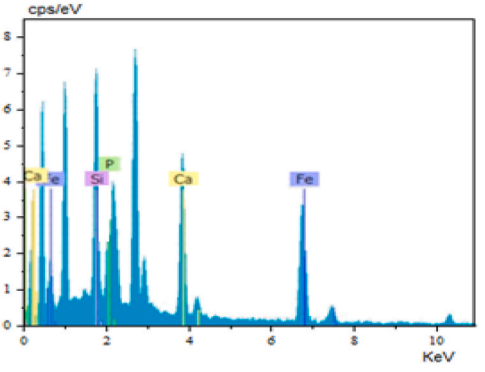

d

(caption on next page)

Fig. 9. SEM images of the G10-G40 glass-ceramic 28 days of immersion in simulated body fluid. The right side of each Fig. shows the elemental composition of the surface. (a) G10F, (b) G20F, (c)G30F and (d) G40F.

4. Conclusion

$(60-x)SiO_2-(10+x)FeO-20CaO-10Na_2O, 0 \leq x \leq 30$ glass-ceramic system were synthesized by sol-gel process. XRD results of samples dried at 110 $^{\circ}C$ showed that the synthesized glasses are completely amorphous. The DTA pattern of the synthesized sample showed two clear crystallization peaks at temperatures of 680 $^{\circ}C$ and 840 $^{\circ}C$. By performing heat treatment at a temperature of 680 $^{\circ}C$, hematite, maghemite, and sodium calcium silicate phases were seen in the glass. With the increment in the FeO percentage in the glass composition, the percentage of maghemite and hematite phases, increased. According to the FTIR spectrum, iron cations in lower amounts ($x \leq 30$) act as glass network former, and in high amounts ($x \geq 30$) act as glass network modifiers. In addition, in SEM images, maghemite and hematite crystals in lower iron oxide percentages are crystallized spherically. But in higher percentages of iron oxide, the morphology of maghemite crystals is dumbbell-shaped, and hematite crystals are cubic-shaped. It was also seen that the size of hematite crystals increased with the increase of iron oxide percentage, but maghemite crystals became smaller.

By performing the heat treatment of the synthesized samples at 840 °C temperature, it was seen that in addition to hematite, maghemite and sodium calcium silicate phases, the wollastonite phase also crystallized in the specimens. By performing treatment at 840 °C, the intensity of hematite peaks incremented, and the intensity of maghemite peaks decremented. Hematite is an antiferromagnetic phase, and increasing the intensity of hematite peaks means reducing the magnetic properties of the samples. In addition, in the structural investigations that in all samples heat treated at 840 °C showed that iron ions act as modifiers in the glass network. Examining of the magnetic properties of the samples, it was also seen that the saturation magnetization of the specimens increment with the increase the iron oxide percentage of the samples. An increment in the saturation magnetization of the samples to higher values indicates an increase in the amount of heat produced under the alternating induction field. In the bioactivity studies, it was seen that all the samples are bioactive. Still the increase in FeO percentage in the composition of the base specimen, the bioactivity of the glass-ceramics decreases.

Author contribution statement

Parisa Rastgoo Oskoui and Mohammad Rezvani: Conceived and designed the experiments; Performed the experiments; Analyzed and interpreted the data; Contributed reagents, materials, analysis tools or data; Wrote the paper.

Data availability statement

Data included in article/sup. material/referenced in article.

Declaration of competing interest

We hereby declare that, we have no affiliations with or involvement in any organization or entity with any financial interest, or non-financial interest in subject matter or materials discussed in this manuscript.

References

[1] K. Mahmoudi, A. Bouras, D. Bozec, R. Ivkov, C. Hadjipanayis, Magnetic hyperthermia therapy for the treatment of glioblastoma: a review of the therapy's history, efficacy and application in humans, Int. J. Hyperther. 34 (8) (2018) 1316–1328, https://doi.org/10.1080/02656736.2018.1430867.
[2] G.P. Skandalakis, D.R. Rivera, C.D. Rizea, A. Bouras, J.G. Jesu Raj, D. Bozec, C.G. Hadjipanayis, Hyperthermia treatment advances for brain tumors, Int. J. Hyperther. 37 (2) (2020) 3–19, https://doi.org/10.1080/02656736.2020.1772512.
[3] S. Gavazzi, A.L. van Lier, C. Zachiu, E. Jansen, J.J.W. Lagendijk, L.J.A. Stalpers, H. Crezee, H.P. Kok, Advanced patient-specific hyperthermia treatment planning, Int. J. Hyperther. 37 (1) (2020) 992–1007, https://doi.org/10.1080/02656736.2020.1806361.
[4] H. Dobšíček Trefná, M. Schmidt, G. Van Rhoon, H. Kok, S. Gordeyev, U. Lamprecht, D. Marder, J. Nadobny, P. Ghadjar, S. Abdel-Rahman, Quality assurance guidelines for interstitial hyperthermia, Int. J. Hyperther. 36 (1) (2019) 276–293, https://doi.org/10.1080/02656736.2018.1564155.
[5] A. Oei, H. Kok, S. Oei, M. Horsman, L. Stalpers, N. Franken, J. Crezee, Molecular and biological rationale of hyperthermia as radio-and chemosensitizer, Adv. Drug Deliv. Rev. 163 (2020) 84–97, https://doi.org/10.1016/j.addr.2020.01.003.
[6] Y. Du, X. Liu, Q. Liang, X.-J. Liang, J. Tian, Optimization and design of magnetic ferrite nanoparticles with uniform tumor distribution for highly sensitive MRI/MPI performance and improved magnetic hyperthermia therapy, Nano Lett. 19 (6) (2019) 3618–3626, https://doi.org/10.1021/acs.nanolett.9b00630.
[7] J. Van Hattum, E. Scutigliani, R. Helderman, R. Zweije, H. Rodermond, A. Oei, J. Crezee, J. Oddens, T. De Reijke, P. Krawczyk, A scalable hyperthermic intravesical chemotherapy (HIVEC) setup for rat models of bladder cancer, Sci. Rep. 12 (1) (2022) 1–11, https://doi.org/10.1038/s41598-022-11016-y.
[8] G. Li, K. Zhang, Z. Pei, N. Zhang, Y. Yu, S. Zhao, G. Liang, J. Zhou, Y. Xing, A novel method to enhance magnetic property of bioactive glass-ceramics for hyperthermia, Ceram. Int. 45 (4) (2019) 4945–4956, https://doi.org/10.1016/j.ceramint.2018.11.194.
[9] P. Ji, Y. Wang, M. Zhang, B. Li, G. Zhang, P2O5-Fe2O3-CaO-SiO2 ferromagnetic glass-ceramics for hyperthermia, Int. J. Appl. Ceram. Technol. 15 (5) (2018) 1261–1267, https://doi.org/10.1111/ijac.12880.
[10] M. Sefidgar, E. Bashooki, P. Shojaee, Numerical simulation of the effect of necrosis area in systemic delivery of magnetic nanoparticles in hyperthermia cancer treatment, J. Therm. Biol. 94 (2020), 102742, https://doi.org/10.1016/j.jtherbio.2020.102742.
[11] O. Sedighi, A. Alaghmandfard, M. Montazerian, F. Baino, A critical review of bioceramics for magnetic hyperthermia, J. Am. Ceram. Soc. 105 (3) (2022) 1723–1747, https://doi.org/10.1111/jace.17861.
[12] M.B. Lodi, Effects of the Inhomogeneous Loading of Magnetic Nanoparticles in Thermoseeds for Bone Tumors Hyperthermia, 2022 3rd URSI Atlantic and Asia Pacific Radio Science Meeting, AT-AP-RASC), IEEE, 2022, pp. 1–4, https://doi.org/10.23919/AT-AP-RASC54737.2022.9814187.

[13] O. Bretcanu, E. Verné, M. Cöisson, P. Tiberto, P. Allia, Temperature effect on the magnetic properties of the coprecipitation derived ferrimagnetic glass-ceramics, J. Magn. Magn Mater. 300 (2) (2006) 412–417, https://doi.org/10.1016/j.jmmm.2005.05.030.

[14] S.A. Shah, M. Hashmi, S. Alam, A. Shamim, Magnetic and bioactivity evaluation of ferrimagnetic ZnFe2O4 containing glass-ceramics for the hyperthermia treatment of cancer, J. Magn. Magn Mater. 322 (3) (2010) 375–381, https://doi.org/10.1016/j.jmmm.2009.09.063.

[15] Y. Wang, B. Li, W. Luo, F. Cao, Bioactivity of Fe2O3-CaO-SiO2 glass-ceramics modified through the addition of P2O5 and TiO2, Ceram. Int. 43 (9) (2017) 6738–6745, https://doi.org/10.1016/j.ceramint.2017.02.080.

[16] W. Leenakul, P. Intawin, T. Tunkasiri, J. Ruangsuriya, K. Pengpat, Preparation of ferrimagnetic BF based silicate glass system, Ceram. Int. 41 (2015) S464–S470, https://doi.org/10.1016/j.ceramint.2015.03.221.

[17] S. El Shabrawy, C. Bocker, C. Rüssel, Crystallization of MgFe2O4 from a glass in the system K2O/B2O3/MgO/P2O5/Fe2O3, Solid State Sci. 60 (2016) 85–91, https://doi.org/10.1016/j.solidstatesciences.2016.08.007.

[18] Y.Y. Wang, B. Li, Y.Y. Wang, Characterization of Fe2O3-CaO-SiO2 Glass-Ceramics Prepared by Sol-Gel, Appl. Mech. Mater., 2014, pp. 114–118, https://doi.org/10.4028/www.scientific.net/AMM.624.114.

[19] F. Baino, E. Fiume, M. Miola, F. Leone, B. Onida, F. Laviano, R. Gerbaldo, E. Verné, Fe-doped sol-gel glasses and glass-ceramics for magnetic hyperthermia, Materials 11 (1) (2018) 173, 10.3390%2Fma11010173.

[20] E. Fiume, C. Migneco, E. Verné, F. Baino, Comparison between bioactive sol-gel and melt-derived glasses/glass-ceramics based on the multicomponent SiO2–P2O5–CaO–MgO–Na2O–K2O system, Materials 13 (3) (2020) 540, https://doi.org/10.3390/ma13030540.

[21] M. Rezvani, P.R. Oskoui, A. Kianvash, Preparation of self-catalyzing sols in the 40SiO2–30FeO–20FeO–20CaO–10Na2O glass system by sol-gel method, ChemistrySelect 8 (6) (2023), https://doi.org/10.1002/slct.202204343.

[22] T. Kokubo, H. Takadama, How useful is SBF in predicting in vivo bone bioactivity? Biomaterials 27 (15) (2006) 2907–2915, https://doi.org/10.1016/j.biomaterials.2006.01.017.

[23] F. Soleimani, M. Rezvani, Addition of alumina to nanoporous calcium titanium phosphate glass-ceramics and its effects on crystallization behavior, Adv. Ceram. Prog. 6 (1) (2020) 36–42, https://doi.org/10.30501/acp.2020.106443.

[24] M. Soleymani Zarabad, M. Rezvani, Investigating the kinetic parameters of SiO2-Al2O3-CaO-CaF2-K2O oxyfluoride glass, Adv. Ceram. Prog. 6 (4) (2020) 1–7, https://doi.org/10.30501/acp.2020.118157.

[25] F. Soleimani, M. Rezvani, The effects of CeO2 addition on crystallization behavior and pore size in microporous calcium titanium phosphate glass-ceramics, Mater. Res. Bull. 47 (6) (2012) 1362–1367, https://doi.org/10.1016/j.materresbull.2012.03.010.

[26] M. Rezvani, B.E. Yekta, V. Marghussian, Utilization of DTA in determination of crystallization mechanism in SiO2–Al2O3–CaO–MgO (R2O) glasses in presence of various nuclei, J. Eur. Ceram. 25 (9) (2005) 1525–1530, https://doi.org/10.1016/j.jeurceramsoc.2004.05.010.

[27] B. Zhao, Y. Wang, H. Guo, J. Wang, Y. He, Z. Jiao, M. Wu, Iron oxide (III) nanoparticles fabricated by electron beam irradiation method, Mater. Sci. -Pol. 25 (4) (2007) 1143–1148, https://doi.org/10.1016/j.materresbull.2012.03.010.

[28] J. Mazo-Zuluaga, C. Barrero, J. Díaz-Terán, A. Jerez, Thermally induced magnetite–haematite transformation, Hyperfine Interact. 148 (1) (2003) 153–161, https://doi.org/10.1023/B:HYPE.0000003776.84005.89.

[29] A.G. Nonaka, M.A. Batista, A.C.S.d. Costa, T.T. Inoue, T.G.M. Bonadio, I.G.d. Souza, Kinetics of thermal transformation of synthetic Al-maghemites into Al-hematites, Rev. Bras. Cienc. Solo. 41 (2017), https://doi.org/10.1590/18069657rbcs20160384.

[30] P.M. Reddy, R. Lakshmi, F.P. Dass, S. Sasikumar, Synthesis, characterization and formulation of sodium calcium silicate bioceramic for drug delivery applications, Sci. Eng. Compos. 23 (4) (2016) 375–380, https://doi.org/10.1515/secm-2014-0057.

[31] Y. Zhao, C. Ning, J. Chang, Sol–gel synthesis of Na2CaSiO4 and its in vitro biological behaviors, J. Sol. Gel Sci. Technol. 52 (1) (2009) 69–74, https://doi.org/10.1007/s10971-009-2038-7.

[32] N.F.B. Pallan, K.A. Matori, M. Hashim, W.F. Lim, H.J. Quah, A. Fauzana, N. Rosnah, M. Khiri, S. Farhana, N. Zainuddin, Preparation of SiO2-Na2O-CaO-P2O5 glass-ceramic from waste materials and heat treatment effects on its morphology, Mater. Sci. Forum (2016) 189–192, https://doi.org/10.4028/www.scientific.net/MSF.846.189.

[33] M. Rezvani, B. Eftekhari-Yekta, M. Solati-Hashjin, V. Marghussian, Effect of Cr2O3, Fe2O3 and TiO2 nucleants on the crystallization behaviour of SiO2–Al2O3–CaO–MgO (R2O) glass-ceramics, l, Ceram. Int. 31 (1) (2005) 75–80, https://doi.org/10.1016/j.ceramint.2004.03.037.

[34] M. Coduri, P. Masala, L. Del Bianco, F. Spizzo, D. Ceresoli, C. Castellano, S. Cappelli, C. Oliva, S. Checchia, M. Allieta, Local structure and magnetism of Fe2O3 maghemite nanocrystals: the role of crystal dimension, Nanomaterials 10 (5) (2020) 867, https://doi.org/10.3390/nano10050867.

[35] T. Hiemstra, Surface structure controlling nanoparticle behavior: magnetism of ferrihydrite, magnetite, and maghemite, Environ. Sci.: Nano 5 (3) (2018) 752–764, https://doi.org/10.1039/C7EN01060E.

[36] D. Flak, Q. Chen, B.S. Mun, Z. Liu, M. Rękas, A. Braun, In situ ambient pressure XPS observation of surface chemistry and electronic structure of α-Fe2O3 and γ-Fe2O3 nanoparticles, Appl. Surf. Sci. 455 (2018) 1019–1028, https://doi.org/10.1016/j.apsusc.2018.06.002.

[37] P.-x. Li, L.-m. Qu, C.-h. Zhang, X.-b. Ren, H.-x. Wang, J.-l. Zhang, Y.-w. Mu, B.-l. Lü, Probing into the crystal plane effect on the reduction of α-Fe2O3 in CO by Operando Raman spectroscopy, J. Fuel Chem. Technol. 49 (10) (2021) 1558–1566, https://doi.org/10.1016/S1872-5813(21)60154-8.

[38] K.-P. Hong, A Geodesic Pair of Magnetic Irreducible Representations in the Hexagonal Chair-Conformer Layer of Hematite.

[39] D. Kubániová, L. Kubíčková, T. Kmječ, K. Závěta, D. Nižňanský, P. Brázda, M. Klementová, J. Kohout, Hematite: morin temperature of nanoparticles with different size, J. Magn. Magn Mater. 475 (2019) 611–619, https://doi.org/10.1016/j.jmmm.2018.11.126.

[40] I.M. Obaidat, S. Alaabed, I.A. Al-Omari, V. Narayanaswamy, B. Issa, A. Khaleel, Field-dependent morin transition and temperature-dependent spin-flop in synthetic hematite nanoparticles, Curr. Nanosci. 16 (6) (2020) 967–975, https://doi.org/10.2174/1573413716666191223124722.

[41] A. Abrajevitch, A.P. Roberts, B.J. Pillans, R.S. Hori, Unexpected magnetic behavior of natural hematite-bearing rocks at low temperatures, G-cubed 22 (12) (2021), e2021GC010094.

[42] M. Rezvani, V.K. Marghussian, B. Eftekhari Yekta, Crystal nucleation and growth rates, time–temperature transformation diagram, and mechanical properties of a SiO2–Al2O3–CaO–MgO–(R2O) glass in the presence of Cr2O3, Fe2O3, and TiO2 nucleants, Int. J. Appl. Ceram. Technol. 8 (1) (2011) 152–162.

[43] C.A. Gorski, M.M. Scherer, Determination of nanoparticulate magnetite stoichiometry by Mossbauer spectroscopy, acidic dissolution, and powder X-ray diffraction: a critical review, Am. Mineral. 95 (7) (2010) 1017–1026.

[44] B. Hehlen, D. Neuville, D. Kilymis, S. Ispas, Bimodal distribution of Si–O–Si angles in sodo-silicate glasses, J. Non-Cryst. Solids 469 (2017) 39–44, https://doi.org/10.1016/j.jnoncrysol.2017.04.009.

[45] M. Rezvani, The effect of complex nucleating agent on the physical and chemical properties of Li2O-Al2O3-SiO2 glass-ceramic, Iran, J. Mater. 7 (4) (2010) 8–15, https://doi.org/10.1016/j.jeurceramsoc.2021.09.034.

[46] A. Velásquez, J. Urquijo, Synthesis and characterization of magnetite-maghemite nanoparticles in presence of polyethylene glycol obtained by mechanical milling, Mater. Sci. Eng. B 263 (2021), 114873, https://doi.org/10.1016/j.mseb.2020.114873.

[47] H. Shokrollahi, A review of the magnetic properties, synthesis methods and applications of maghemite, J. Magn. Magn Mater. 426 (2017) 74–81, https://doi.org/10.1016/j.jmmm.2016.11.033.

[48] D. Kargin, Y.V. Konyukhov, A. Biseken, A. Lileev, D.Y. Karpenkov, Structure, morphology and magnetic properties of hematite and maghemite nanopowders produced from rolling mill scale, Steel Transl. 50 (3) (2020) 151–158, https://doi.org/10.3103/S0967091220030055.

[49] B.D. Cullity, C.D. Graham, Introduction to Magnetic Materials, John Wiley & Sons, 2011.

[50] Y. Liu, K. Xue, S. Yao, Structure, degradation and hydroxyapatite conversion of B-doped 58S bioglass and glass-ceramics, J. Ceram. Soc. Jpn. 127 (4) (2019) 232–241, https://doi.org/10.2109/jcersj2.18206.

[51] E.P.-I. Erasmus, Synthesis, Testing and Characterization of Porous Biocompatible Porous Bioactive Glasses for Clinical Use, PhD diss, 2017.